Single-domain (110) PbTiO3 thin films: Thermodynamic theory and experiments

P Mtebwa, P K Tagantsev, T Yamada, N Setter, P. Gemeiner, B. Dkhil

Single-domain (110) $PbTiO_3$ thin films: Thermodynamic theory and experiments

M. Mtebwa,[1,*] A. K. Tagantsev,[1] T. Yamada,[2,3] P. Gemeiner,[4] B. Dkhil,[4] and N. Setter[1,†]

[1]*Ceramics Laboratory, Swiss Federal Institute of Technology (EPFL), CH-1015 Lausanne, Switzerland*

[2]*Department of Materials, Physics and Energy Engineering, Nagoya University, Nagoya 464-8603, Japan*

[3]*PRESTO, Japan Science and Technology Agency, 4-1-8 Honcho, Kawaguchi, Saitama 332-0012, Japan*

[4]*Laboratoire Structures, Propriétés et Modélisation des Solides, UMR8580, Centre Nationale de la Recherche Scientifique, Centrale Supélec Université Paris-Saclay, 92295 Châtenay-Malabry Cedex, France*

(Received 20 May 2015; revised manuscript received 27 January 2016; published 14 April 2016)

We report the thermodynamic potential for single-domain (110) thin films epitaxially grown on dissimilar cubic substrates. Using different sets of paraelectric phase elastic compliance coefficients of $PbTiO_3$ single crystal, calculated from the experimental room-temperature values, we predict rotational phases similar to those observed in (001) thin films under anisotropic biaxial misfit strain. The new sets of elastic compliance coefficients also predict a triclinic phase that could potentially lead to the enhancement of both dielectric and piezoelectric properties. We also conducted experimental studies on highly tetragonal monocrystalline $PbZr_{0.05}Ti_{0.95}O_3$ thin films of different thicknesses, epitaxially grown on (110) $SrTiO_3$ substrate by pulsed laser deposition technique. Piezoresponse force microscopy measurements showed that the as-grown films were single domain with the a_2c phase, which corroborates with the prediction of the theory. Moreover, the T_c values of both thin and thick films (17–90 nm) also fell within the predicted range (540–600 °C). The measured remanet polarization of 57 $\mu C/cm^2$ was in good agreement with the theoretical values of 55–58 $\mu C/cm^2$. Small-signal piezoelectric response measurements gave a piezoelectric coefficient of 40 pm/V, which is also in good agreement with the numerically calculated values of 38–42 pm/V.

DOI: 10.1103/PhysRevB.93.144113

I. INTRODUCTION

Substrate clamping in thin films is known to result in anisotropic internal stresses in the film material. Consequently, phase-transition temperatures, temperature-domain states, stability range, symmetry, and the type of the transition in the film are expected to be different from those of the bulk [1–3].

The effect of substrate clamping on thin-film properties has also been predicted through thermodynamic calculations based on both single-domain [4–9] and polydomain [10,11] theories as well as first-principles calculations [12].

Despite the fact that polydomain (twinned) states predicted by the polydomain theory have been shown to substantially modify the thin-film phase diagrams [10,11,13], single-domain approximation still provides acceptable predictions. For instance T_c values for cubic to tetragonal *out-of-plane* phase transition for both $Pb(Zr_{0.1}Ti_{0.9})O_3$ and $Pb(Zr_{0.2}Ti_{0.8})O_3$ predicted by single-domain theory [6] are in agreement with those predicted by polydomain theory [11]. Moreover, the difference in the energy of the film-substrate interface for different domain states may favor the single-domain state over the polydomain state [7].

While there is extensive literature on phase diagrams of (001) oriented ferroelectric thin films, and to a lesser extent on (111) oriented films [7], single-domain thermodynamic theory of (110) oriented ferroelectric thin films has not been reported. In contrast to the (001) orientation, the (110) clamping can potentially result in further reduction of the symmetry of the high-temperature phase, which may in turn influence stability of room-temperature phases as well as their physical and electrical properties.

Despite the fact that different sets of experimental room-temperature (ferroelectric phase) elastic compliances have been reported in the literature [14–17], most of the reported thermodynamic calculations involving $PbTiO_3$ (PTO) use only high-temperature (paraelectric phase) elastic compliance values that were reported by Pertsev *et al.* [4]. However, it has been shown that values of elastic compliances can potentially affect the phase diagrams of thin films [18,19]. These observations justify the recalculation of paraelectric phase elastic compliance values from different sets of the experimental room-temperature values, which eventually allows us to study their impact on the misfit-temperature phase diagram of $PbTiO_3$.

In this work we develop a single-domain thermodynamic potential of (110) oriented ferroelectric thin film from which the temperature-misfit strain phase diagrams are determined and the electrical properties are calculated. The choice of PTO is justified by the fact that it is one of the most studied ferroelectrics with single-crystal experimental parameters needed for thermodynamic calculation that are readily available. We also performed experimental studies on the highly tetragonal monocrystalline $Pb(Zr_{0.05}Ti_{0.95})O_3$ (PZT 05/95) thin films epitaxially grown on (110) $SrTiO_3$ single-crystal substrates to validate our theoretical predictions.

The layout of this paper is as follows. We start with the development of the single-domain thermodynamic potential for (110) thin film in Sec. II. Section III presents the derivation of the expressions for calculating paraelectric phase elastic compliances from room-temperature experimental values and tabulates the four sets of elastic compliances of PTO single crystal that were used in the subsequent thermodynamic calculations. Developed phase diagrams are then presented and discussed in Sec. IV. Details of the phase diagrams include both the stable phases and their respective point groups and

*mahamudu.mtebwa@epfl.ch

†nava.setter@epfl.ch

the discussion is focused on the comparisons with (001) films and the effect of elastic compliances. Section V is devoted to the numerical calculation of the small-signal dielectric and piezoelectric responses as a function of misfit strain at room temperature. Processing procedures and structural properties of (110) PZT 05/95 thin films are presented in Sec. VI. The processing part is only briefly presented; for detailed explanations the reader is referred to Appendix A. Finally the comparison between the theoretical predictions and experimental values of T_c as well as electrical properties of PZT 05/95 are presented and discussed in Secs. VII and VIII, respectively.

II. THERMODYNAMIC POTENTIAL OF (110) ORIENTED EPITAXIAL THIN FILMS

Stable thermodynamic states of short circuited perovskite bulk ferroelectric crystals are usually obtained through minimization of the standard elastic Gibbs energy function of a cubic ferroelectric given by the expansion

$$\begin{aligned} G = {} & \alpha_1\left(\tilde{P}_1^2+\tilde{P}_2^2+\tilde{P}_3^2\right)+\alpha_{11}\left(\tilde{P}_1^4+\tilde{P}_2^4+\tilde{P}_3^4\right) \\ & +\alpha_{12}\left(\tilde{P}_1^2\tilde{P}_2^2+\tilde{P}_1^2\tilde{P}_3^2+\tilde{P}_2^2\tilde{P}_3^2\right) \\ & +\alpha_{111}\left(\tilde{P}_1^6+\tilde{P}_2^6+\tilde{P}_3^6\right)+\alpha_{112}\left[\tilde{P}_1^4\left(\tilde{P}_2^2+\tilde{P}_3^2\right)\right. \\ & \left.+\tilde{P}_2^4\left(\tilde{P}_1^2+\tilde{P}_3^2\right)+\tilde{P}_3^4\left(\tilde{P}_1^2+\tilde{P}_2^2\right)\right] \\ & +\alpha_{123}\tilde{P}_1^2\tilde{P}_2^2\tilde{P}_3^2-\tfrac{1}{2}s_{11}\left(\tilde{\sigma}_1^2+\tilde{\sigma}_2^2+\tilde{\sigma}_3^2\right) \\ & -s_{12}(\tilde{\sigma}_1\tilde{\sigma}_2+\tilde{\sigma}_1\tilde{\sigma}_3+\tilde{\sigma}_2\tilde{\sigma}_3) \\ & -\tfrac{1}{2}s_{44}\left(\tilde{\sigma}_4^2+\tilde{\sigma}_5^2+\tilde{\sigma}_6^2\right)-Q_{11}\left(\tilde{\sigma}_1\tilde{P}_1^2+\tilde{\sigma}_2\tilde{P}_2^2+\tilde{\sigma}_3\tilde{P}_3^2\right) \\ & -Q_{12}\left[\tilde{\sigma}_1\left(\tilde{P}_2^2+\tilde{P}_3^2\right)+\tilde{\sigma}_2\left(\tilde{P}_1^2+\tilde{P}_3^2\right)+\tilde{\sigma}_3\left(\tilde{P}_1^2+\tilde{P}_2^2\right)\right] \\ & -Q_{44}(\tilde{P}_1\tilde{P}_2\tilde{\sigma}_6+\tilde{P}_1\tilde{P}_3\tilde{\sigma}_5+\tilde{P}_2\tilde{P}_3\tilde{\sigma}_4) \end{aligned} \tag{1}$$

where $\tilde{P}_i$ and $\tilde{\sigma}_i$ are components of polarization vector and stress tensor in Voigt notation and in the crystal reference frame aligned with the cubic axes of the material ($\tilde{X}_1$, $\tilde{X}_2$, $\tilde{X}_3$). The temperature dependence is introduced by the dielectric stiffness $\alpha_1 = (T - T_0)/2\varepsilon_0 C$ where T_0, C, and ε_0 are Curie-Weiss temperature, Curie-Weiss constant, and vacuum permittivity, respectively. All higher-order dielectric stiffness coefficients α_{ij} and α_{ijk} are taken as temperature independent. It is important to also note that the influence of high-order electromechanical coupling terms [20] is neglected. We also use the notation $Q_{44} = 4Q_{1212}$ following Ref. [21].

Transformation of the free energy from the crystal reference frame ($\tilde{X}_1$, $\tilde{X}_2$, $\tilde{X}_3$) to the (110) film reference frame (X_1, X_2, X_3) shown in Fig. 1 is implemented through transforming both polarization P_i and stress σ_i components in Eq. (1) by using the transformation laws $\tilde{P}_i = A_{ij}P_j$ and $\tilde{\sigma}_{ij} = A_{ik}A_{jl}\sigma_{kl}$, respectively, where A_{ij} is the transformation matrix given as [22] (hereafter the dummy suffix summation convention is adopted)

$$A_{ij} = \begin{pmatrix} 1 & 0 & 0 \\ 0 & 1/\sqrt{2} & -1/\sqrt{2} \\ 0 & 1/\sqrt{2} & 1/\sqrt{2} \end{pmatrix}. \tag{2}$$

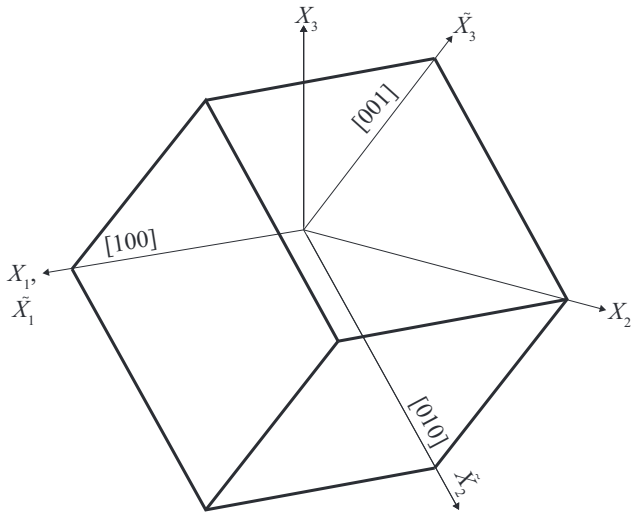

FIG. 1. Crystal and film reference frames for a (110) clamped thin film. Transformation is performed from the crystal reference frame ($\tilde{X}_1$, $\tilde{X}_2$, $\tilde{X}_3$) aligned with the cubic axes of the material to the film reference frame (X_1, X_2, X_3).

Then it follows that the effective thermodynamic potential for a single-domain ferroelectric thin film on a thick substrate is given as [6]

$$G_{\text{eff}} = G + u_1\sigma_1 + u_2\sigma_2 + u_6\sigma_6. \tag{3}$$

The mixed mechanical boundary conditions in the film reference frame entail the assumption of symmetric biaxial misfit strain $u_1 = u_2 = u_m$ and $u_6 = 0$ and zero stress acting on the film free surface, i.e., $\sigma_3 = \sigma_4 = \sigma_5 = 0$ [6]. The remaining stress components in Eq. (1) can then be eliminated by using the elastic equation of state:

$$u_i = -\partial G/\partial\sigma_i. \tag{4}$$

After rewriting Eq. (1) in the film reference frame and then using Eq. (3), the effective thermodynamic potential for (110) oriented ferroelectric film which is a function of polarization vector $\mathbf{P}$, misfit strain u_m, and temperature T is finally given as

$$\begin{aligned} G_{\text{eff}}(\mathbf{P},u_m,T) = {} & \alpha_{1a}^*P_1^2+\alpha_{1b}^*P_2^2+\alpha_3^*P_3^2+\alpha_{11}^*P_1^4+\alpha_{22}^*P_2^4 \\ & +\alpha_{33}^*P_3^4+\alpha_{12}^*P_1^2P_3^2+\alpha_{13}^*P_1^2P_3^2 \\ & +\alpha_{23}^*P_2^2P_3^2+\alpha_{111}P_1^6+\alpha_{111a}^*\left(P_2^6+P_3^6\right) \\ & +\alpha_{112}\left[P_1^4\left(P_2^2+P_3^2\right)\right] \\ & +\alpha_{112}^*\left[P_2^4\left(P_1^2+P_3^2\right)+P_3^4\left(P_1^2+P_2^2\right)\right] \\ & +a_{123}^*P_1^2P_2^2P_3^2+U^*u_m^2 \end{aligned} \tag{5}$$

where

$$\alpha_{1a}^* = \alpha_1 - u_m\frac{[(2Q_{11}+4Q_{12})(s_{11}-s_{12})+Q_{11}s_{44}]}{2s_{11}^2-4s_{12}^2+s_{11}(2s_{12}+s_{44})}, \tag{6}$$

$$\alpha_{1b}^* = \alpha_1 - u_m\frac{[(2Q_{11}+4Q_{12}+Q_{44})(s_{11}-s_{12})+Q_{12}s_{44}]}{2s_{11}^2-4s_{12}^2+s_{11}(2s_{12}+s_{44})}, \tag{7}$$

$$\alpha_3^* = \alpha_1 - u_m \frac{[(2Q_{11} + 4Q_{12} - Q_{44})(s_{11} - s_{12}) + Q_{12}s_{44}]}{2s_{11}^2 - 4s_{12}^2 + s_{11}(2s_{12} + s_{44})}. \tag{8}$$

The rest of the renormalized temperature-independent coefficients can be found in Appendix B. It can also be noted that the expression for α_3^* in Eq. (8) is identical to that obtained by Schmidt *et al.* [22] for the (110) film reference frame.

III. ELASTIC COMPLIANCES OF LEAD TITANATE SINGLE CRYSTAL

In this section we develop the expressions that relate the paraelectric phase elastic compliances of a ferroelectric crystal to the experimental room-temperature values, so that we can use the literature data to calculate new sets of elastic compliance coefficients for $PbTiO_3$ single crystal in the paraelectric phase.

Starting with evaluation of s_{11} and s_{12}, the application of $\tilde{\sigma_1} = \tilde{\sigma_2} = \tilde{\sigma_3}$ does not lead to polarization rotation, hence we perform renormalization by taking into account the variation of P_3 only. The derivation starts by substituting the solution for tetragonal $PbTiO_3$, i.e., $\tilde{P}_1^2 = \tilde{P}_2^2 = 0$, $\tilde{P}_3^2 \neq 0$ into the free energy of the bulk crystal [Eq. (1)] and then applying the equation of state $\partial G/\partial \tilde{P}_3 = 0$ to get

$$2\alpha_1\tilde{P}_3 + 4\alpha_{11}\tilde{P}_3^3 + 6\alpha_{111}\tilde{P}_3^5 - 2\tilde{P}_3 Q_{12}(\tilde{\sigma_1} + \tilde{\sigma_2}) - 2\tilde{P}_3 Q_{11}\tilde{\sigma_3} = 0. \tag{9}$$

The nonzero solution to this equation at zero stress, $\tilde{P}_3 \equiv P_s$, yields the value of the spontaneous polarization. For small stresses, Eq. (9) can be linearized by applying small perturbation $\delta\tilde{P}_3$, such that $\tilde{P}_3 = P_s + \delta\tilde{P}_3$, where P_s is the spontaneous polarization. By neglecting higher-order terms of $\delta\tilde{P}_3$ and $\delta\tilde{P}_3\tilde{\sigma_i}$ terms after expansion, we obtain

$$\begin{aligned}&\left(2\alpha_1 P_s + 4\alpha_{11}P_s^3 + 6\alpha_{111}P_s^5\right) \\ &\quad + \delta P_3\left(2\alpha_1 + 12\alpha_{11}P_s^2 + 30\alpha_{111}P_s^4\right) \\ &\quad = 2P_s Q_{12}(\tilde{\sigma_1} + \tilde{\sigma_2}) + 2P_s Q_{11}\tilde{\sigma_3},\end{aligned} \tag{10}$$

where the first term is zero since P_s is the equilibrium value of the order parameter (equation of state, $\frac{\partial G}{\partial \tilde{P}_3}|_{\tilde{P}_3 = P_s} = E = 0$). And after rearranging, Eq. (10) becomes

$$\delta\tilde{P}_3 = \frac{P_s}{\chi^{-1}}(Q_{12}(\tilde{\sigma_1} + \tilde{\sigma_2}) + Q_{11}\tilde{\sigma_3}) \tag{11}$$

where χ is the dielectric susceptibility given by

$$\chi^{-1} = \alpha_1 + 6\alpha_{11}P_s^2 + 15\alpha_{111}P_s^4. \tag{12}$$

In addition, from the strain equation (4), we have the following strain tensor relationships:

$$u_1 = \frac{\delta G}{\delta\tilde{\sigma_1}} = \tilde{P}_3^2 Q_{12} + s_{11}\tilde{\sigma_1} + s_{12}(\tilde{\sigma_2} + \tilde{\sigma_3}) \tag{13}$$

and

$$u_3 = \frac{\delta G}{\delta\tilde{\sigma_3}} = \tilde{P}_3^2 Q_{11} + s_{12}(\tilde{\sigma_1} + \tilde{\sigma_2}) + s_{11}\tilde{\sigma_3}. \tag{14}$$

Similarly, we analyze the linear strain response to small variations $\delta\tilde{P}_3$ by substituting $\tilde{P}_3 = P_s + \delta\tilde{P}_3$ in Eqs. (13) and (14) with $\delta\tilde{P}_3$ coming from Eq. (11) to obtain, neglecting higher order terms,

$$\begin{aligned}\delta u_1 &= u_1 - P_s^2 Q_{12} \\ &= s_{11}\tilde{\sigma_1} + s_{12}(\tilde{\sigma_2} + \tilde{\sigma_3}) \\ &\quad + \frac{2P_s^2}{\chi^{-1}}\left[Q_{12}^2(\tilde{\sigma_1} + \tilde{\sigma_2}) + Q_{11}Q_{12}\tilde{\sigma_3}\right]\end{aligned} \tag{15}$$

and

$$\begin{aligned}\delta u_3 &= u_3 - P_s^2 Q_{11} \\ &= s_{11}\tilde{\sigma_3} + s_{12}(\tilde{\sigma_1} + \tilde{\sigma_2}) \\ &\quad + \frac{2P_s^2}{\chi^{-1}}\left[Q_{11}Q_{12}(\tilde{\sigma_1} + \tilde{\sigma_2}) + Q_{11}^2\tilde{\sigma_3}\right].\end{aligned} \tag{16}$$

Then we use the relation $s'_{ij} = \delta u_i/\delta\tilde{\sigma_j}$ to obtain the following expressions for the corrected ferroelectric phase ($T < T_c$) elastic compliances;

$$\begin{aligned}s'_{11} &= s_{11} + AQ_{12}^2, \\ s'_{12} &= s_{12} + AQ_{12}^2, \\ s'_{13} &= s_{12} + AQ_{11}Q_{12}, \\ s'_{33} &= s_{11} + AQ_{11}^2,\end{aligned} \tag{17}$$

where the coefficient $A = \frac{2P_s^2}{\chi^{-1}}$ that can be calculated from the experimental parameters is also introduced. Finally, solving the set of equation, Eq. (17), we express two electrostriction coefficients and two paraelectric phase elastic compliances in terms of the experimental room temperature elastic compliances as follows

$$\begin{aligned}Q_{11} &= -\frac{(s'_{11} - s'_{12} + s'_{13} - s'_{33})}{[A(s'_{33} - s'_{11} + 2(s'_{12} - s'_{13}))]^{1/2}}, \\ Q_{12} &= -\frac{(s'_{12} - s'_{13})}{[A(s'_{33} - s'_{11} + 2(s'_{12} - s'_{13}))]^{1/2}}\end{aligned} \tag{18}$$

$$\begin{aligned}s_{11} &= \frac{s'_{11} + s'_{33} - A\left(Q_{12}^2 - Q_{11}^2\right)}{2}, \\ s_{12} &= \frac{s'_{12} + s'_{13} - A\left(Q_{12}^2 - Q_{11}Q_{12}\right)}{2}.\end{aligned} \tag{19}$$

To evaluate s_{44} and Q_{44}; we take into account the following. $\tilde{\sigma}_6$ does not lead to linear response with respect to the polarization and thus $s'_{66} = s_{44}$. In contrast, $\tilde{\sigma}_4$ and $\tilde{\sigma}_5$ result into variations with respect to P_1 and P_2. Thus by applying similar renormalization procedures with respect to $\delta\tilde{P}_1$ and $\delta\tilde{P}_2$, we get

$$s'_{44} = s_{44} + \frac{P_s^2}{2\chi_{13}^{-1}}Q_{44}^2 \tag{20}$$

where $\chi_{13}^{-1} = \alpha_1 + \alpha_{12}P_s^2 + \alpha_{112}P_s^4$.

Thus, relations (18), (19) and (20) enable us to calculate the paraelectric phase elastic compliances and electrostriction coefficients of PTO, basing on the available experimental data. In our calculation we have used the three available sets of experimental room temperature s'_{ij} coefficients given in Table I and a value of $A = 1.1 \times 10^{-9}$ $C^4N^{-1}m^{-6}$ estimated by using $T = 25\,^\circ C$, $T_0 = 478\,^\circ C$, $C = 1.5 \times 10^5\,^\circ C$ and $P_s = 81$ Cm^{-2}, for PTO [15,23] single crystal. The results of the calculations are summarized in Table II where the Q_{ij}

TABLE I. Coefficients used in the thermodynamic calculations of PTO. s'_{ij} are the experimentally measured room-temperature elastic coefficients for the PTO single crystal.

Coefficient (PTO)	Ref. [23]	Ref. [17]	Ref. [16]	Ref. [14]
α_1[Jm C^2]	$3.76648(T-478.474)x10^5$			
α_{11}[Jm^5 C^{-4}]	-7.253×10^7			
α_{12}[Jm^5 C^{-4}]	7.500×10^8			
α_{111}[Jm^9 C^{-6}]	2.606×10^8			
α_{112}[Jm^9 C^{-6}]	6.100×10^8			
α_{123}[Jm^9 C^{-6}]	-3.660×10^9			
Q_{11}[m^4 C^{-2}]	8.9×10^{-2}			
Q_{12}[m^4 C^{-2}]	-2.6×10^{-2}			
Q_{44}[m^4 C^{-2}]	9.6×10^{-2}			
s'_{11}[10^{-12} Pa^{-1}]		6.5	7.1	7.2
s'_{33}[10^{-12} Pa^{-1}]		33.3	21.3	32.5
s'_{12}[10^{-12} Pa^{-1}]		−0.35	−0.4	−2.1
s'_{13}[10^{-12} Pa^{-1}]		−7.1	−6.3	−8.0
s'_{44}[10^{-12} Pa^{-1}]		14.5	15.4	12.2
s'_{66}[10^{-12} Pa^{-1}]		9.6	9.6	7.9

coefficients from Haun *et al.* [23] and s_{ij} coefficients from Pertsev *et al.* [4] have also been included for comparison. An appreciable spread of the data given in this table is seen. For example, the s_{11} and s_{12} coefficients from Pertsev *et al.* [4] are significantly different from the calculated values.

IV. PHASE DIAGRAMS

Phase diagrams are constructed from the components of the equilibrium polarization states of a single-domain film at a given temperature and misfit strain through minimization of Eq. (5) by using coefficients from Table I together with the four sets of elastic compliance coefficients from Table II. In this calculations, we neglect the residual depolarizing field due to possible incomplete screening under the assumption that the films are sandwiched between short circuited electrodes [6], consistent with experiments [24]. It is also assumed that no relaxation through the formation of ferroelastic domains occurs.

Stable rotational phases are defined in terms of *zero* and *nonzero* polarization components as shown in Fig. 2. Spontaneous polarization P_S is along X_3 for the c phase ($P_1 = P_2 = 0, P_3 \neq 0$), confined in the X_2-X_3 plane for the a_2c phase ($P_1 = 0, P_2 \neq P_3 \neq 0$) and the $r^\star$ phase ($P_1 \neq P_2 \neq 0, P_2 \neq P_3 \neq 0, P_3 \neq P_1 \neq 0$), confined in the X_1-X_2 plane for the a_1a_2 phase ($P_1 \neq P_2 \neq 0, P_3 = 0$), and along X_1 for the a_1 phase ($P_1 \neq 0, P_2 = P_3 = 0$). A paraelectric phase is assigned when all polarization components are zero, i.e., $P_1 = P_2 = P_3 = 0$.

Figure 3 shows the phase diagrams obtained from four different sets of elastic compliances (Table II). For detailed description of the phase diagrams, we also developed Fig. 4 to show the origin of all possible phases. Each single-domain phase can be viewed as the phase of the free standing film with polarization rotated by the misfit strain imposed by the substrate. The resulting relationships were used to identify the symmetries of all phases indicated in parentheses in Fig. 3.

All figures differ remarkably from the phase diagram of single-domain (001) $PbTiO_3$ under isotropic biaxial misfit strain [4].

(110) PTO thin-film phase diagrams determined using elastic compliances in set I [Fig. 3(a)] and II [Fig. 3(b)] of Table II predict six phases while with set III [Fig. 3(c)] and IV [Fig. 3(d)] of Table II one finds five phases instead of four observed in (001) PTO thin films. Three phases, namely, a, a_2c, and a_1a_2, are common in all four cases and were only predicted in (001) PTO thin film under anisotropic biaxial misfit strain condition [25]. The extra phase $r^\star$ with triclinic symmetry in Figs. 3(a) and 3(b) was also predicted in (001) film only under anisotropic biaxial misfit strain [25]. Prediction of the triclinic phase instead of the monoclinic r phase

TABLE II. Paraelectric phase elastic compliance coefficients calculated from room-temperature experimental values reported in the literature (Table I) by using Eqs. (18)–(20). s_{ij} values in columns I–III were calculated using room-temperature data from Refs. [14,16,17]. In addition, s_{ij} and Q_{ij} values from Pertsev *et al.* [4] and Haun *et al.* [23], respectively, are also shown for comparison purposes.

	Calculated values			For comparison	
	I	II	III	IV (Pertsev *et al.* [4])	V (Haun et al. [23])
s_{11}[10^{-12} Pa^{-1}]	5.4	5.8	6.3	8.0	
s_{12}[10^{-12} Pa^{-1}]	−1.5	−1.7	−3.0	−2.5	
s_{44}[10^{-12} Pa^{-1}]	9.6	9.6	7.9	9.0	
Q_{11}[10^{-2} m^4 C^{-2}]	15.9	11.9	15.4		8.9
Q_{12}[10^{-2} m^4 C^{-2}]	−3.2	−3.5	−2.9		−2.6
Q_{44}[10^{-2} m^4 C^{-2}]	9.3	10.2	8.7		9.6

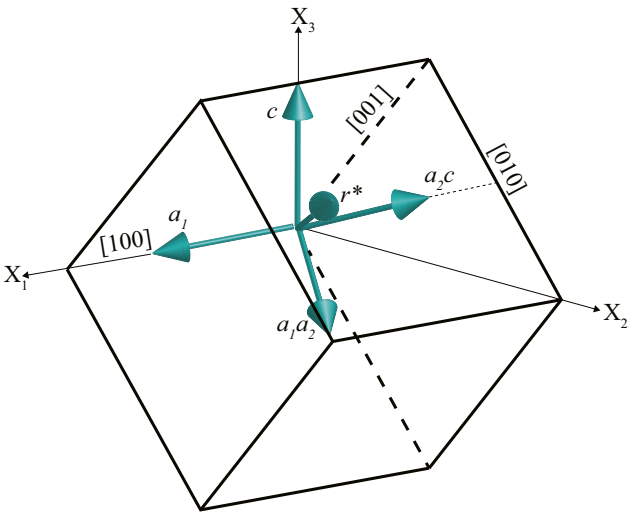

FIG. 2. Orientation of the spontaneous polarization P_S, in a (110) clamped single-domain ferroelectric thin film: c phase ($P_1 = P_2 = 0, P_3 \neq 0$), a_2c phase ($P_1 = 0, P_2 \neq P_3 \neq 0$), $r^\star$ phase ($P_1 \neq P_2 \neq 0, P_2 \neq P_3 \neq 0, P_3 \neq P_1 \neq 0$), a_1a_2 phase ($P_1 \neq P_2 \neq 0, P_3 = 0$), and a_1 phase ($P_1 \neq 0, P_2 = P_3 = 0$).

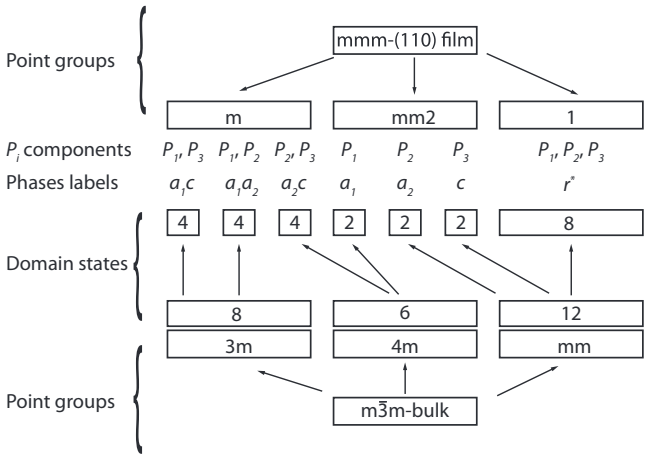

FIG. 4. Relationships between point-group symmetries and domain states of all possible phases in the (110) clamped thin film. a_1a_2 and a_2c phases which were both predicted by the developed phase diagrams share the same point symmetry group m but have different polarization components.

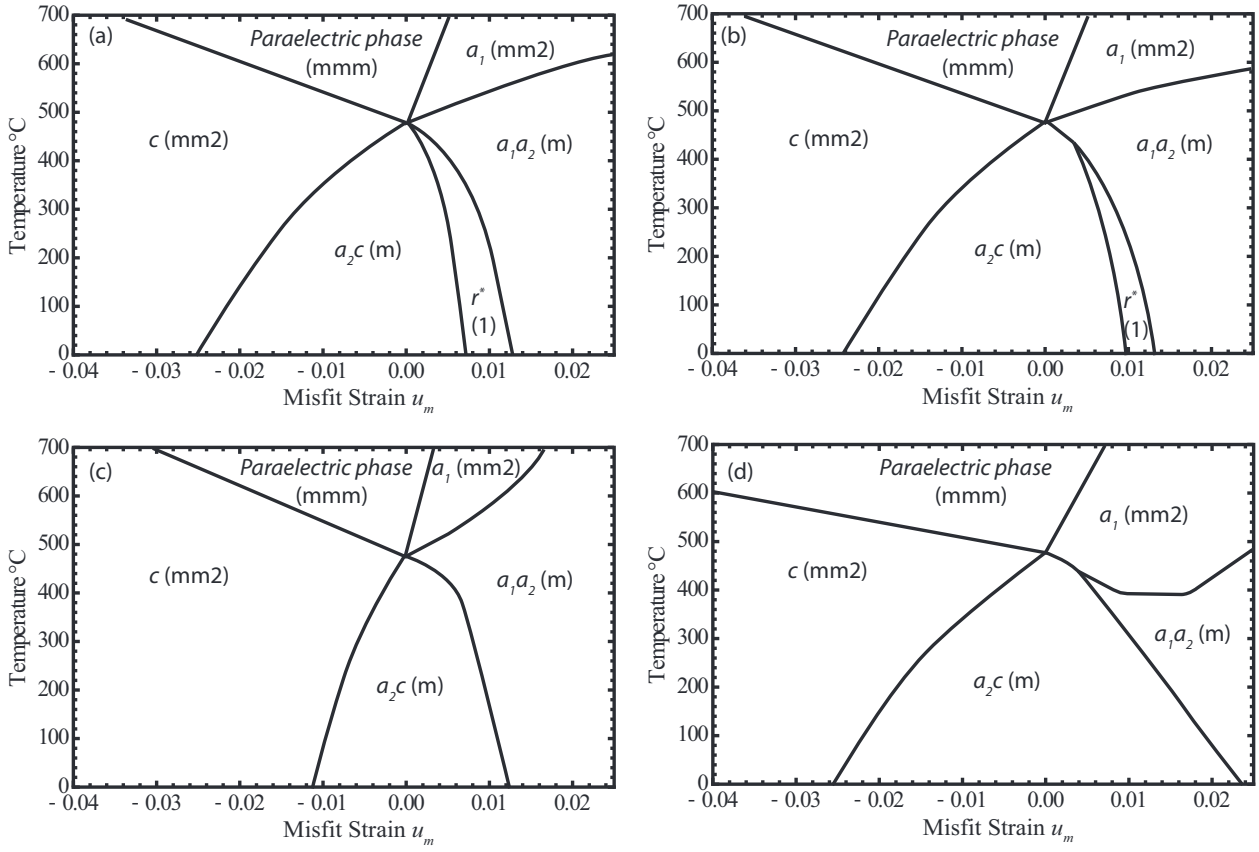

FIG. 3. Temperature-parent misfit strain phase diagrams of single-domain (110) $PbTiO_3$ thin film calculated by using elastic compliances in column I (a), II (b), III (c), and IV (Pertsev *et al.* [4]) (d) of Table II. The point-group symmetries corresponding to each phase are also indicated in brackets. The value of temperature at $u_m = 0$ corresponds to the Curie-Weiss temperature T_0 of the stress free $PbTiO_3$ crystal. The effects of the values of elastic compliances include the shift of phase boundaries and differences in number of stable phases. Phases previously predicted in single-domain (001) $PbTiO_3$ thin film under anisotropic misfit strain [25] are also predicted here.

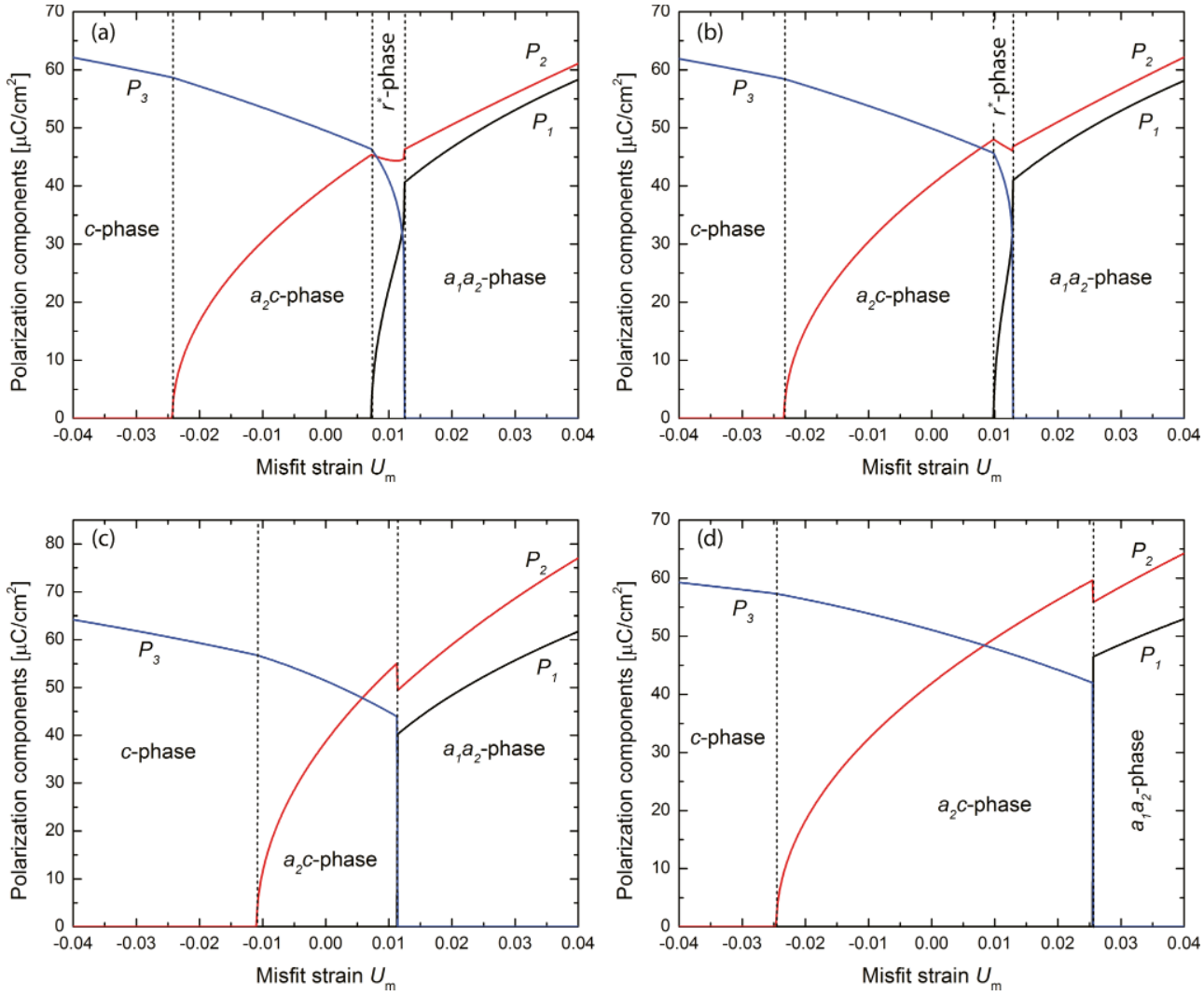

FIG. 5. Polarization-misfit strain diagrams of a single-domain (110) $PbTiO_3$ thin film calculated by using elastic compliances in column I (a), II (b), III (c), and IV (d) of Table II.

($P_1 = P_2 \neq 0, P_3 \neq 0$) previously simulated under isotropic biaxial misfit strain condition [4] is due to the following symmetry reasons. The (110) film clamping seems to produce the same effect as anisotropic biaxial misfit strain, namely it lowers the symmetry of the paraelectric phase from $m\bar{3}m$ (in the bulk) down to mmm. Consequently, also the symmetries of the ferroelectric phases are lower than those of (001) films. It is also important to note that the positions of phase boundaries of the phase diagram based on the mostly used Pertsev elastic compliance set [Fig. 3(d)] are remarkably different from those of the other three figures.

The nature of the phase transitions for the predicted room-temperature phases is clearly shown by the polarization-misfit strain diagrams which we also calculated using the four sets of elastic compliances (Fig. 5). All four figures are characterized by second order c-a_2c transitions at the onset of P_2. Figures 5(a) and 5(b) also show second order a_2c-$r^\star$ transitions at the onset of P_1. As for the onset of P_3 at the $r^\star$-a_1a_2 phase boundary, the transition is close to continuous in Figs. 5(a) and 5(b) while a sharp evolution of both P_1 and P_3 in both Figs. 5(c) and 5(d) suggests well pronounced first order transitions.

Single-domain theory predictions are known to fail on account of ferroelastic domains [10,26]. Thus, potentially significant changes in the phase diagram are expected when a polydomain theory is used instead. Nevertheless, the predictions for the $PbTiO_3$ phase diagram region corresponding to compressive misfit strain are not expected to be influenced much when the polydomain theory is employed [10].

V. DIELECTRIC AND PIEZOELECTRIC PROPERTIES

The calculation of both the dielectric permittivity and piezoelectric coefficients of a single-domain film is limited to small signal responses ($\mathbf{E} \rightarrow 0$), and thus only equilibrium polarization components at zero electric field $\mathbf{E}$ are used [6]. The determination of the dielectric permittivity $\varepsilon_{ij} = \varepsilon_b \delta_{ij} + \eta_{ij}$ (where δ_{ij} is a kronecker delta and ε_b is the background permittivity), proceeds by first deriving the expression for reciprocal dielectric susceptibilities $\eta_{ij}^{-1} = \partial G_{\text{eff}}(u_m, T)/\partial P_i \partial P_j$ and then applying the matrix

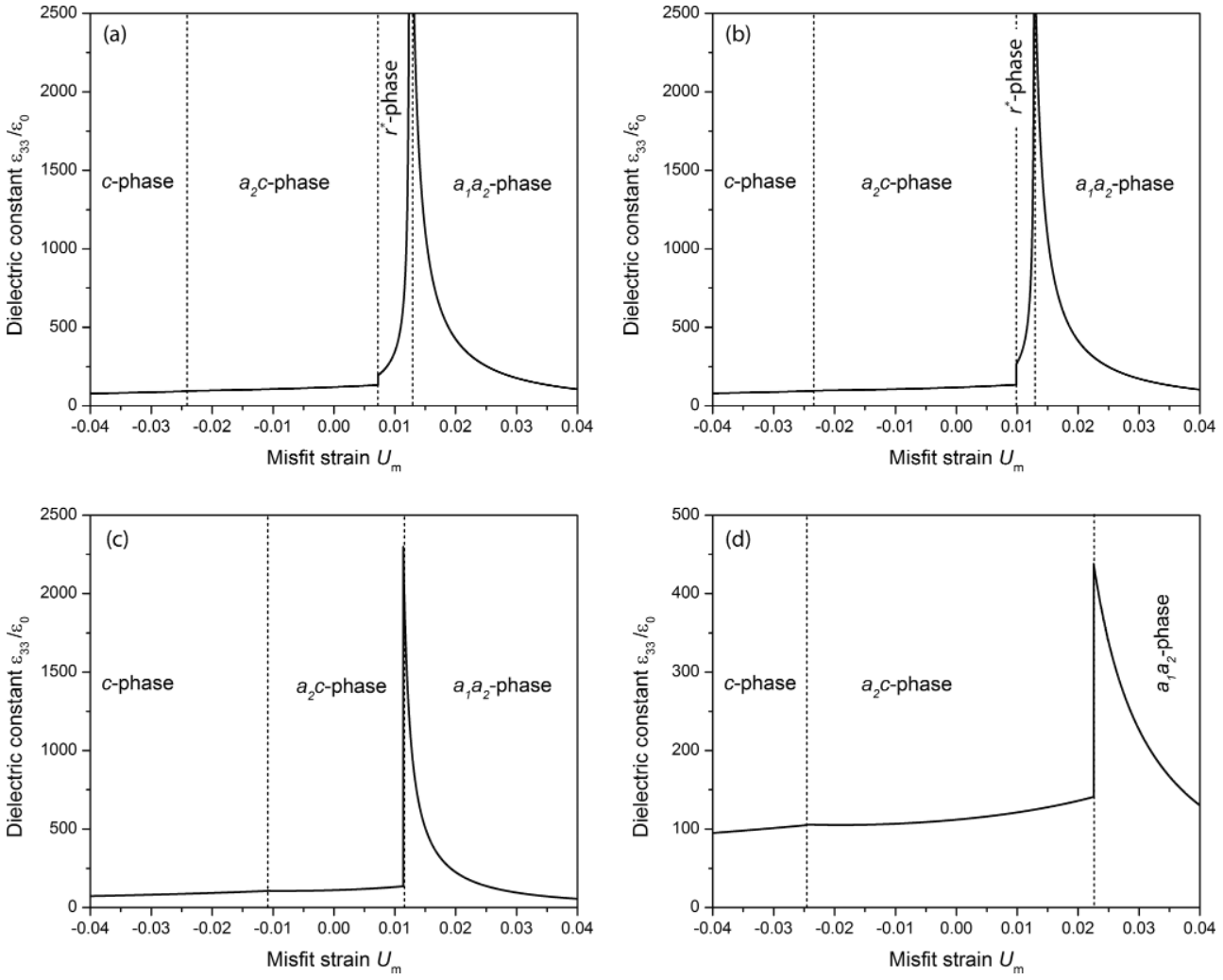

FIG. 6. Out-of-plane small-signal dielectric responses as a function misfit strain at 25 °C for a single-domain (110) $PbTiO_3$ thin film calculated by using elastic compliances in column I (a), II (b), III (c), and IV (d) of Table II. Polarization rotation in the $r^\star$ phase in figures (a) and (b) predicts much higher values of dielectric constants.

inversion. Using the obtained dielectric susceptibilities, the small-signal piezoelectric coefficients d_{ij} are then calculated from $d_{ij} = b_{kj}\eta_{ki}$, where $b_{kj} = \partial u_j/\partial P_k$. In this work only small-signal out-of-plane dielectric permittivities ε_{33} as well as piezoelectric coefficients d_{33}, that can in practice be measured by using a conversional parallel plate capacitor configuration, were calculated.

Figures 6 and 7 show both calculated out-of-plane dielectric constant $\varepsilon_r = \varepsilon_{33}/\varepsilon_0$ and piezoelectric coefficient d_{33}, respectively, as a function of misfit strain for the four sets of elastic compliance values. In Fig. 6 it can be seen that for all four cases the values of dielectric constants for c, a_2c, and a_1a_2 (at higher u_m) are comparable; however, the presence of the $r^\star$ phase in Figs. 6(a) and 6(b) predicts much higher values, similar to the prediction by Pertsev *et al.* [4] for (001)PTO films (although in their case a monoclinic r phase was involved). A similar trend is observed in the piezoelectric responses (Fig. 7), however in this case the absence of the $r^\star$ phase in Figs. 7(c) and 7(d) remarkably predicts no divergence of the piezoelectric coefficient at the a_1a_2-phase boundary. This observation suggests that piezoelectric response is potentially more sensitive to the elastic compliance values relative to the dielectric response. Relative dielectric responses at $r^\star$-a_1a_2 transitions in Figs. 6(a) and 6(b) and Figs. 6(c) and 6(d) suggest second- and first-order phase transitions consistent with the corresponding polarization-misfit strain diagrams (Fig. 5). High dielectric responses observed in Figs. 6(a) and 6(b) can be explained by the polarization rotation within the $r^\star$ phase (see Fig. 5).

VI. THIN-FILM PROCESSING AND STRUCTURAL CHARACTERIZATION

Validation of the thermodynamic calculations was conducted on highly tetragonal (110) oriented $PbZr_{0.05}Ti_{0.95}O_3$ (PZT 05/95) thin films, 17–100 nm thick, grown on (110) $SrTiO_3$ (STO) substrate by pulsed laser deposition (PLD) as detailed in Appendix A. Monocrystalline structure and pure (110) out-of-plane films orientation were confirmed by both transmission electron microscopy (TEM) and x-ray-diffraction (XRD) measurements as shown in Fig. 8(a). In addition,

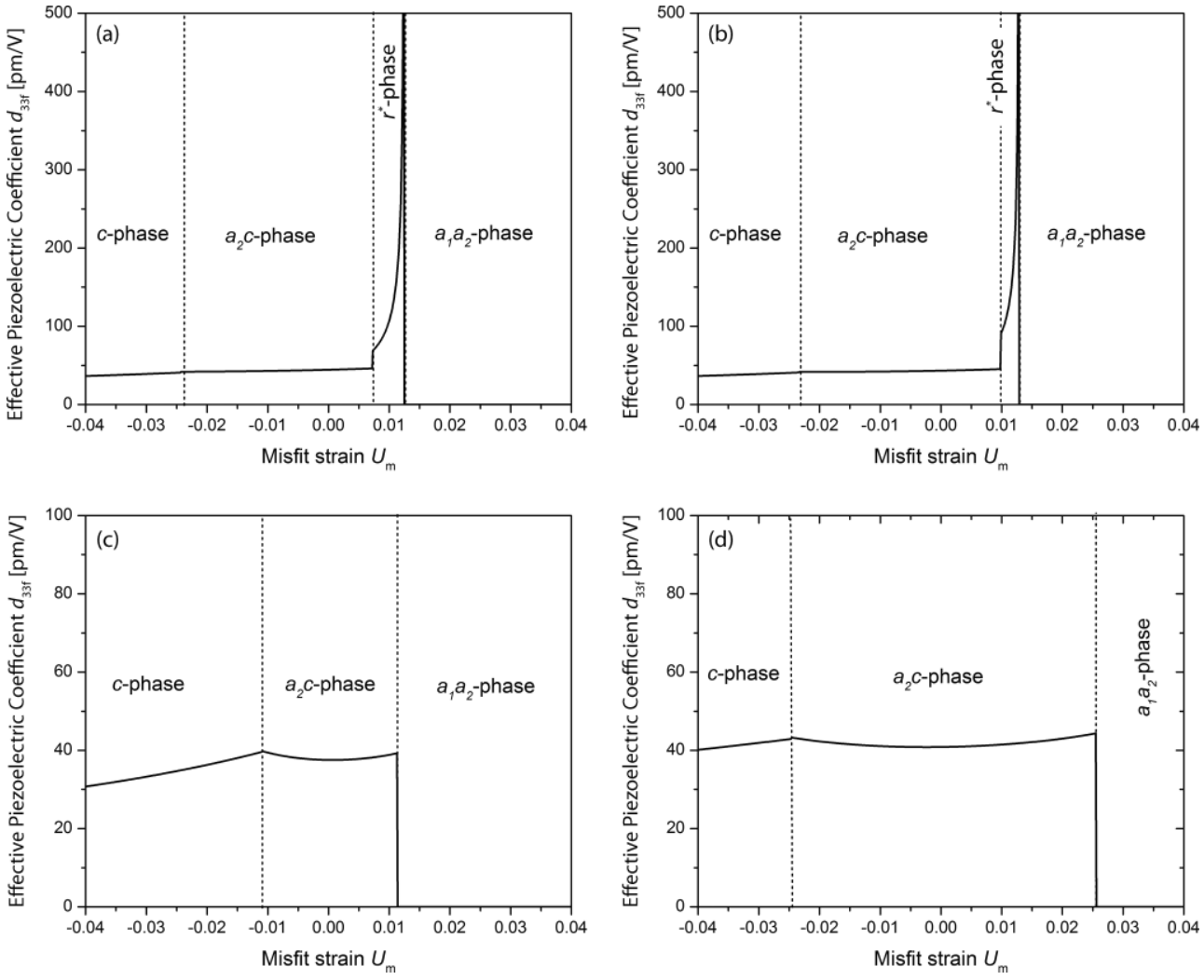

FIG. 7. Out-of-plane small-signal piezoelectric responses as a function of misfit strain at 25 °C for a single-domain (110) $PbTiO_3$ thin film calculated by using elastic compliances in column I (a), II (b), III (c), and IV (d) of Table II. Polarization rotation in the $r^\star$ phase in figures (a) and (b) predicts much higher values of piezoelectric coefficients while almost zero divergence is observed in figures (c) and (d).

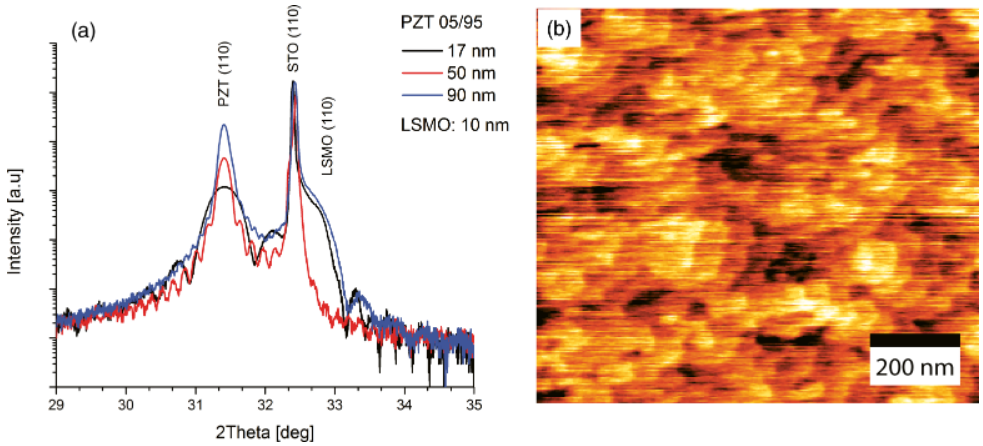

FIG. 8. 2Theta XRD scan for (110) peak of 17-, 50-, and 90-nm (110) PZT 05/95 thin films (a) and AFM topography of a 50-nm (110) PZT 05/95 film (b). All films were grown on STO(110) with 10-nm LSMO. Films have the roughness of about 0.15 nm (root mean square). Thickness fringes on XRD image and terraces observed on AFM topography suggest good quality films with highly controlled growth modes.

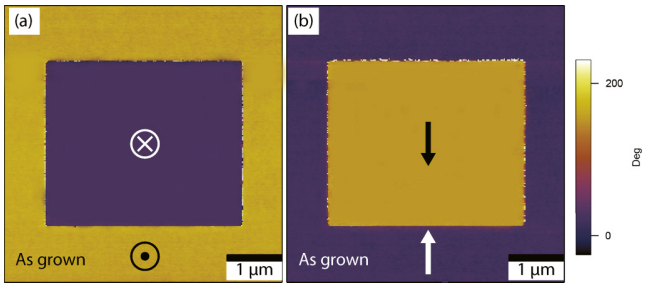

FIG. 9. Vertical (a) and lateral (b) PFM phases of a 50-nm (110) PZT 05/95 film grown on STO(110) with 10-nm LSMO. PFM images indicate upwards as-grown monodomain structure and the downwards poled central area which switched by applying 5 V on the AFM tip. Vertical and lateral PFM images were used to reconstruct the as-grown single-domain orientation. The orientation of the spontaneous polarization in our single-domain films suggests that we have a a_2c phase (see Fig. 10).

terraces observed on atomic force microscopy (AFM) topography [Fig. 8(b)] suggested well-controlled film growth mode.

Domain structures in the films were studied by both piezoresponse force microscopy (PFM) and XRD reciprocal space maps (RSM). PFM images (Fig. 9) taken on areas of up to 30 × 30 μm confirmed that our films are predominantly of single-domain state with the orientation shown schematically in Fig. 10, the configuration of which is consistent with the a_2c phase [see Fig. 2(b)]. The out-of-plane polarization of thinner films (17 nm) was downwards (i.e., pointing towards the substrate) whereas that of thicker films (□ 30 nm) was upwards as shown in Fig. 9(a).

VII. PHASE-TRANSITION TEMPERATURE (T_c) MEASUREMENTS

Figures 11(a)–11(c) show temperature evolution of the lattice parameters of 17-, 50-, and 90-nm-thick (110) PZT 05/95 thin films, together with pseudocubic bulk values extrapolated from the value of $PbTiO_3$ and $PbZr_{0.2}Ti_{0.8}O_3$ [27–29]. The results shown correspond to the lattice period in the out-of-plane direction divided by $\sqrt{2}$ (see Fig. 10). Measured phase-transition temperatures were approximately 550 °C for a 17-nm film, 567 °C for a 50-nm film, and 580 °C for a 90-nm film, all much higher than the bulk value (483 °C) as expected.

Figure 11(d) shows both experimental data and theoretical predictions for single-domain (110) $PbTiO_3$ thin film calculated by using elastic compliances from columns I–IV of

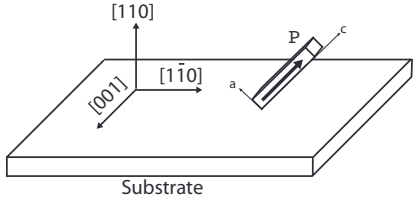

FIG. 10. Schematics of polarization orientation in single-domain (110) tetragonal thin film. Polarization orientation corresponds to the a_2c phase predicted in Sec. IV.

Table II. The experimental parent misfit strain [30] $u_m = (a_s - a_{pc})/a_s$ was estimated by using the room-temperature in-plane film lattice parameter a_s, and the cubic lattice parameter of the free standing film (bulk) a_{pc} extrapolated to room temperature. The a_s values measured at room temperature as well as the extrapolated a_{pc} values are, respectively, indicated by blue rectangles and solid black lines in Figs. 11(a) and 11(b).

It is seen that the indicated experimental points fall within the predicted range of the paraelectric-c phase transition temperature irrespective of the film thicknesses. These observations are in agreement with the theoretical predictions obtained using three out of four sets of elastic compliances, namely s_{ij} values from column I, II, and IV of Table II. It is also remarkable that the same three sets of s_{ij} imply the a_2c phase at room temperature which is consistent with the PFM observations. All these findings suggest that sets I, II, and IV of elastic compliances provides a better description of PTO elasticity. However, the accuracy of our data on the temperature dependence of the out-of-plane lattice constant does not enable us to identify the c to the a_2c phase transition, which must have take place on cooling down from the paraelectric to the a_2c phase.

VIII. ELECTRICAL CHARACTERIZATION

Electrical measurements were conducted on a film capacitor with 5.0% Nb doped ST(110) as bottom electrode and 600-μm-diameter Pt top electrode. The rather large top electrode is necessary for the piezoelectric measurements by the *double laser beam interferometer*. Piezoelectric measurements were conducted at 5 kHz, 0.1 V ac small signal with 1-s pulse.

A. Polarization hysteresis loop

Figure 12(a) shows the measured polarization-electric field hysteresis loop of a 100-nm (110) PZT 05/95 thin film. The film has coercive fields of $E_C^+ = 138$ kV/cm and $E_C^- = 53$ kV/cm, maximum polarization $P_{max} = 87\,\mu C/cm^2$, and remanent polarization $Pr = 57\,\mu C/cm^2$. Figure 12(b) indicates good agreement between the theoretical results and experimental remanent polarization value at the corresponding film misfit strain value ($\approx -1.6 \times 10^{-2}$).

B. Effective piezoelectric coefficient ($d_{33,f}$)

Figure 13 shows the $d_{33,f}$ measurements as a function of applied electric field together with the comparison with theoretical calculations. Theoretical predictions have shown that the shape of the piezoelectric loop can be influenced by the type of contribution to the converse piezoelectric effect [31]. The absence of a *hump* and *nose* (loop opening) at high fields in Fig. 13(a) clearly suggests intrinsic contribution as the dominant mechanism for piezoelectricity, and thus further confirms the single-domain state of our films. Figure 13(b) shows a remarkable agreement between the experimental and predicted values of the piezoelectric coefficient.

IX. SUMMARY AND CONCLUSIONS

Single-domain thermodynamic theory was used to develop a temperature-misfit strain phase diagram of (110) $PbTiO_3$ thin film under isotropic biaxial misfit strain. In parallel, the expressions for calculating paraelectric phase elastic compliances

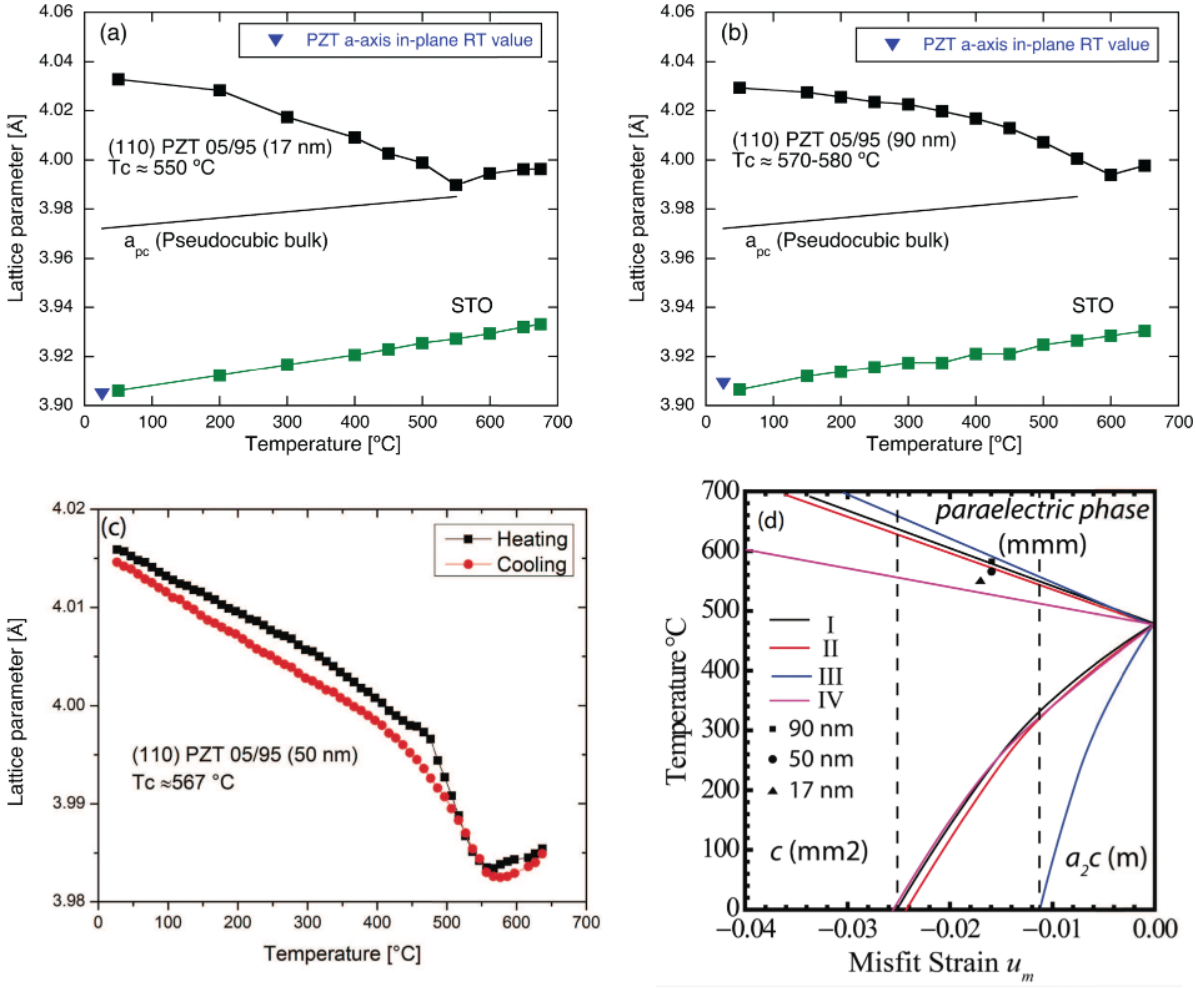

FIG. 11. Measurements of phase-transition temperatures of (110) PZT 05/95 thin films grown on STO(110) substrate. Film thickness 17 nm showing $T_C = 550\,^{\circ}$C (a), film thickness 90 nm showing $T_C = 570$–$580\,^{\circ}$C (b), and film thickness 50 nm showing $T_C = 567\,^{\circ}$C (c). The (110) lattice spacings times $\sqrt{2}$ are shown as the out-of-plane lattice parameters of PZT films. The a_s values measured at room temperature as well as the extrapolated a_{pc} values are, respectively, indicated by blue rectangles and solid black lines in (a) and (b). (d) shows comparison with theoretical predictions. The theoretical curves correspond to values obtained using the four sets (I, II, III, and IV) of s_{ij} corresponding to columns I, II, III, and IV of Table II. The dashed lines show the interval of the misfit strain where sets I, II, and III imply the a_2/c phase at room temperature while set IV implies the c phase.

from ferroelectric phase values were derived, from which three new sets of elastic compliances were calculated. Contrary to the single-domain (001) $PbTiO_3$ thin-film phase diagram, and depending upon values of elastic compliances used, the (110) phase diagram predicts up to five rotational phases instead of four, only three of which were predicted in (001) $PbTiO_3$ thin films under anisotropic misfit strain condition. The types of phases and phase boundary positions were found to be affected by elastic compliance coefficients similar to previous reports [19]. Using the newly calculated elastic compliances we predicted the triclinic $r^{\star}$ which in turn predicts anomalous enhancement of both dielectric and piezoelectric properties at the critical misfit strain. It should be noted that this phase was previously predicted in (001) $PbTiO_3$ thin films only under anisotropic misfit strain primarily because of the reduced symmetry of the high-temperature phase [25].

Our experimental studies on the highly tetragonal monocrystalline PZT 05/95 thin films epitaxially grown on STO(110) substrates are in good agreement with theoretical predictions. PFM measurements showed that the as-grown films were single domain with the a_2c phase. Measured T_c values (550–580 °C) were higher than the bulk values (483 °C) and fell within the predicted range (540–600 °C). Remanet polarization of 57 μC/cm^2 was in good agreement with theoretical values 55–58 μC/cm^2. Furthermore, the measured small-signal piezoelectric coefficient of 40 pm/V was close to the theoretical value of 38–42 pm/V.

The comparison of the results of our modeling with our experimental results suggests that of the four sets of data for the values of elastic compliancies for PTO in the paraelectric phase given in Table II sets I, II, and III provides a better description of PTO elasticity. This follows from the fact that

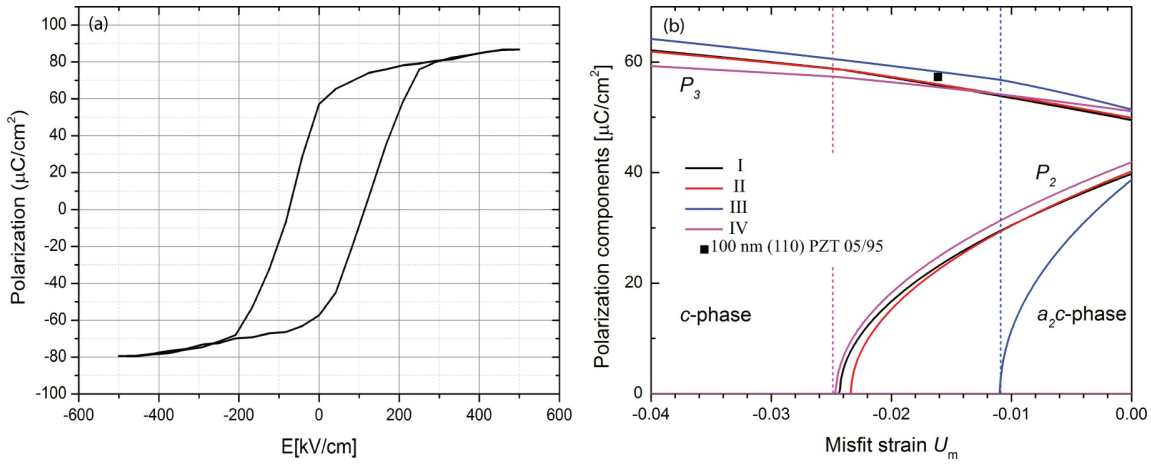

FIG. 12. Polarization measurements of (110) PZT 05/95 thin films grown on STO(110) substrate. Experimental hysteresis loop (a) and comparison with theoretical predictions (b). In figure (b), the four lines indicate theoretical values calculated using the four different sets of elastic compliances (see Table II). The measured remanet polarization of 57 $\mu C/cm^2$ is in good agreement with the theoretical values (55–58 $\mu C/cm^2$).

the calculations basing on these sets predict the a_2c phase at room temperature, documented by our PFM data, while set IV predicts the c phase. Unfortunately, we do not have any information on the presence of the r^* phase, which could have enabled further assessment of the validity of the sets of elastic compliances. Concerning the above discussion, one should keep in mind its limitation due to the neglect of high-order electrostrictions [20] in the framework employed in our calculations.

ACKNOWLEDGMENTS

Financial support was received from the Swiss National Science foundation (Switzerland) and the Lithuanian-Swiss cooperation program (Switzerland) to reduce economic and social disparities within the enlarged European Union under Project Agreement No. CH-3-ŠMM-01/02. T.Y. was supported by the Japan Society for the Promotion of Science (Japan) KAKENHI Grant No. 26709047 and JST-PRESTO.

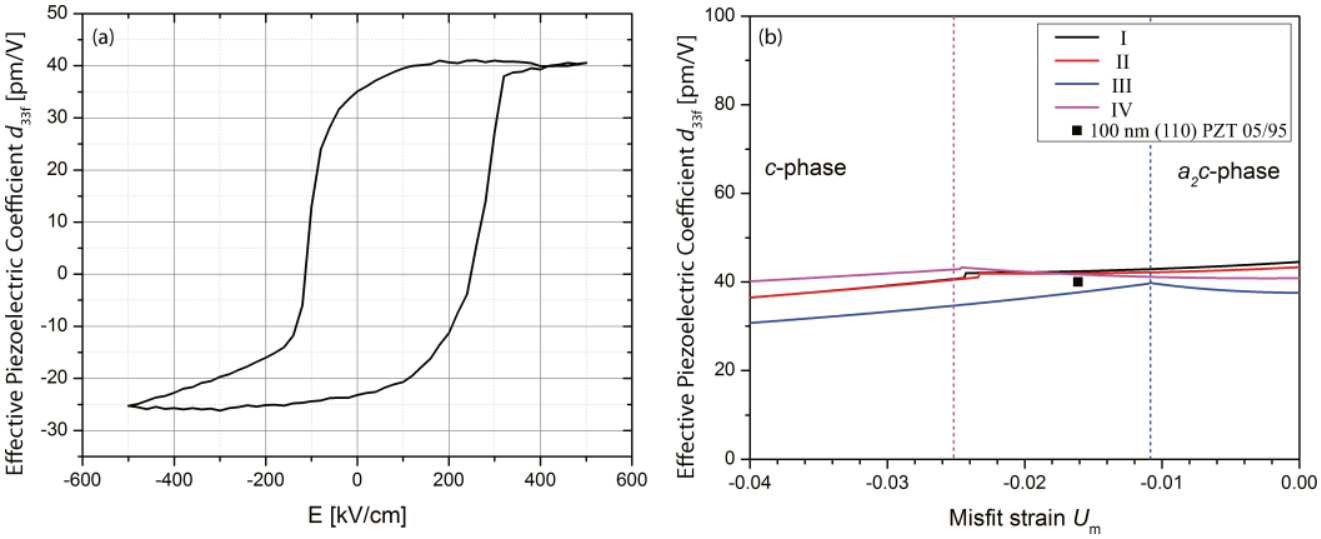

FIG. 13. Effective piezoelectric coefficient measurement of (110) PZT 05/95 thin films grown on STO(110) substrate. Piezoelectric hysteresis loop (a) and comparison with theoretical predictions (b). In figure (b), the four lines indicate theoretical values calculated using the four different sets of elastic compliances (see Table II). The measured effective piezoelectric coefficient of 40 pm/V is in good agreement with the numerically calculated values of 38–42 pm/V. The shape of the experimental loop suggests intrinsic contribution as the dominant mechanism for piezoelectricity.

APPENDIX A: THIN-FILM PROCESSING

Highly tetragonal $PbZr_{0.05}Ti_{0.95}O_3$ (PZT 05/95) thin films of different thicknesses (17–130 nm) were grown on undoped STO(110) (STO) substrate (supplied by Crystal GmbH, Germany) with about a 10-nm LSMO bottom electrode as well as on 5% Nb doped STO(110) by PLD from a self-made PZT 05/95 target. The PLD system used had a laser wavelength of 248 nm, and the laser energy density used was 1 J/cm^{-2}. Deposition parameters were 620 °C growth temperature, 112-mTorr O_2 pressure, and 2 Hz for LSMO; and 550 °C, 200 mTorr, and 3 Hz for PZT. All films were cooled at oxygen pressure of 2.0 Torr.

In this work PZT 05/95 was chosen because targets for pure $PbTiO_3$ composition could not be easily sintered due to cracking resulting from the high spontaneous strain that develops during paraelectric-ferroelectric phase transition. In addition, while commercial $PbTiO_3$ targets are readily available, this option was not considered due to uncertainty regarding their processing conditions. At room temperature, PZT 05/95 ($a = 0.3916$ nm, $c = 0.4142$ nm) has a mismatch of about -0.27 and -3.21% along [100] and [1$\bar{1}$0] directions of the STO($a = 3.905$ nm) substrate, respectively. The film bulk lattice parameter of 0.3985 nm at growth temperature, obtained by interpolating the available bulk values and thermal expansion coefficients of $PbTiO_3$ and other PZT compositions [15,27–29], gives average mismatch of about -1.4% with STO ($a \approx 0.393$ nm at 550 °C).

APPENDIX B: RENORMALIZED TEMPERATURE-INDEPENDENT COEFFICIENTS FOR EQ. (5)

$$\alpha_{11}^* = \alpha_{11} + \frac{4Q_{12}^2 s_{11} - 8Q_{11}Q_{12}s_{12} + Q_{11}^2[2(s_{11}+s_{12})+s_{44}]}{4s_{11}^2 - 8s_{12}^2 + 2s_{11}(2s_{12}+s_{44})}, \tag{B1}$$

$$\alpha_{22}^* = \frac{2\alpha_{11}+\alpha_{12}}{4} + \frac{(4Q_{11}^2+Q_{44}^2+4Q_{11}Q_{44})s_{11}}{8\left[2s_{11}^2 - 4s_{12}^2 + s_{11}(2s_{12}+s_{44})\right]} + \frac{(8Q_{11}Q_{12}+4Q_{12}Q_{44})(s_{11}-2s_{12}) + 4Q_{12}^2(3s_{11}-2s_{12}+s_{44})}{8\left[2s_{11}^2 - 4s_{12}^2 + s_{11}(2s_{12}+s_{44})\right]}, \tag{B2}$$

$$\alpha_{33}^* = \frac{2\alpha_{11}+\alpha_{12}}{4} + \frac{\left(4Q_{11}^2+Q_{44}^2-4Q_{11}Q_{44}\right)s_{11}}{8\left[2s_{11}^2 - 4s_{12}^2 + s_{11}(2s_{12}+s_{44})\right]} + \frac{(8Q_{11}Q_{12}-4Q_{12}Q_{44})(s_{11}-2s_{12}) + 4Q_{12}^2(3s_{11}-2s_{12}+s_{44})}{8[2s_{11}^2 - 4s_{12}^2 + s_{11}(2s_{12}+s_{44})]}, \tag{B3}$$

$$\alpha_{12}^* = \alpha_{12} + \frac{Q_{12}[Q_{44}s_{11} + 2Q_{12}(s_{11}-2s_{12})] - 2Q_{11}^2 s_{12}}{2s_{11}^2 - 4s_{12}^2 + s_{11}(2s_{12}+s_{44})} + \frac{Q_{11}[-Q_{44}s_{12} + Q_{12}(4s_{11}+s_{44})]}{2s_{11}^2 - 4s_{12}^2 + s_{11}(2s_{12}+s_{44})} + \frac{Q_{44}^2}{2s_{44}}, \tag{B4}$$

$$\alpha_{13}^* = \alpha_{12} + \frac{Q_{12}[-Q_{44}s_{11} + 2Q_{12}(s_{11}-2s_{12})] - 2Q_{11}^2 s_{12}}{2s_{11}^2 - 4s_{12}^2 + s_{11}(2s_{12}+s_{44})} + \frac{Q_{11}[Q_{44}s_{12} + Q_{12}(4s_{11}+s_{44})]}{2s_{11}^2 - 4s_{12}^2 + s_{11}(2s_{12}+s_{44})}, \tag{B5}$$

$$\alpha_{23}^* = \frac{6\alpha_{11}-\alpha_{12}}{2} + \frac{4Q_{11}^2 s_{11} - Q_{44}^2 s_{11} + 8Q_{11}Q_{12}(s_{11}-2s_{12})}{4\left[2s_{11}^2 - 4s_{12}^2 + s_{11}(2s_{12}+s_{44})\right]} + \frac{4Q_{12}^2(3s_{12}-2s_{12}+s_{44})}{4\left[2s_{11}^2 - 4s_{12}^2 + s_{11}(2s_{12}+s_{44})\right]}, \tag{B6}$$

$$\alpha_{111a}^* = \frac{\alpha_{111}+\alpha_{112}}{4}, \quad \alpha_{112}^* = \frac{2\alpha_{112}+\alpha_{123}}{4}, \quad \alpha_{123}^* = \frac{6\alpha_{112}+\alpha_{123}}{2}, \tag{B7}$$

$$U^* = \frac{6(s_{11}-s_{12})+s_{44}}{4(s_{11}-s_{12})(s_{11}+2s_{12}) + 2s_{11}s_{44}}. \tag{B8}$$

[1] P.-E. Janolin, B. Fraisse, F. Le Marrec, and B. Dkhil, Appl. Phys. Lett. **90**, 212904 (2007).

[2] P.-E. Janolin, F. Le Marrec, J. Chevreul, and B. Dkhil, Appl. Phys. Lett. **90**, 192910 (2007).

[3] A. Bartasyte, B. Dkhil, J. Kreisel, J. Chevreul, O. Chaix-Pluchery, L. Rapenne-Homand, C. Jiménez, A. Abrutis, and F. Weiss, Appl. Phys. Lett. **93**, 242907 (2008).

[4] N. A. Pertsev, A. G. Zembilgotov, and A. K. Tagantsev, Phys. Rev. Lett. **80**, 1988 (1998).

[5] N. A. Pertsev, Z. G. Zembilgotov, and A. K. Tagantsev, Ferroelectrics **223**, 79 (1999).

[6] N. A. Pertsev, V. G. Kukhar, H. Kohlstedt, and R. Waser, Phys. Rev. B **67**, 054107 (2003).

[7] A. K. Tagantsev, N. A. Pertsev, P. Muralt, and N. Setter, Phys. Rev. B **65**, 012104 (2001).

[8] F. A. Urtiev, V. G. Kukhar, and N. A. Pertsev, Appl. Phys. Lett. **90**, 252910 (2007).

[9] M. Mtebwa, A. K. Tagantsev, and N. Setter, AIP Adv. **4**, 127150 (2014).

[10] V. G. Koukhar, N. A. Pertsev, and R. Waser, Phys. Rev. B **64**, 214103 (2001).

[11] V. G. Kukhar, N. A. Pertsev, H. Kohlstedt, and R. Waser, Phys. Rev. B **73**, 214103 (2006).

[12] O. Diéguez and D. Vanderbilt, Phase Transitions **81**, 607 (2008).

[13] Q. Y. Qiu, V. Nagarajan, and S. P. Alpay, Phys. Rev. B **78**, 064117 (2008).

[14] V. Gavrilya and E. Fesenko, Soviet Physics Crystallography, USSR **16**, 549 (1971).

[15] T. Mitsui, K.-H. Hellwege, and A. M. Hellwege, *Numerical Data and Functional Relationships in Science and Technology.*

Group III, Crystal and Solid State Physics. V. 16, Ferroelectrics and Related Substances. Non-Oxides (Springer-Verlag, Berlin, 1982).

[16] Z. Li, M. Grimsditch, X. Xu, and S.-K. Chan, Ferroelectrics **141**, 313 (1993).

[17] A. Kalinichev, J. Bass, B. Sun, and D. Payne, J. Mater. Res. **12**, 2623 (1997).

[18] J. H. Haeni, P. Irvin, W. Chang, R. Uecker, P. Reiche, Y. L. Li, S. Choudhury, W. Tian, M. E. Hawley, B. Craigo *et al.*, Nature (London) **430**, 758 (2004).

[19] V. B. Shirokov, Y. I. Yuzyuk, B. Dkhil, and V. V. Lemanov, Phys. Rev. B **75**, 224116 (2007).

[20] A. Kvasov and A. K. Tagantsev, Phys. Rev. B **87**, 184101 (2013).

[21] M. Davis, M. Budimir, D. Damjanovic, and N. Setter, J. Appl. Phys. **101**, 054112 (2007).

[22] S. Schmidt, J. Lu, S. P. Keane, L. D. Bregante, D. O. Klenov, and S. Stemmer, J. Am. Ceram. Soc. **88**, 789 (2005).

[23] M. Haun, Z. Zhuang, E. Furman, S. Jang, and L. E. Cross, Ferroelectrics **99**, 45 (1989).

[24] M. Dekkers, M. D. Nguyen, R. Steenwelle, P. M. Te Riele, D. H. A. Blank, and G. Rijnders, Appl. Phys. Lett. **95**, 012902 (2009).

[25] A. G. Zembilgotov, N. A. Pertsev, U. Böttger, and R. Waser, Appl. Phys. Lett. **86**, 052903 (2005).

[26] N. A. Pertsev and H. Kohlstedt, Phys. Rev. Lett. **98**, 257603 (2007).

[27] G. Shirane and S. Hoshino, J. Phys. Soc. Jpn. **6**, 265 (1951).

[28] M. J. Haun, Ph.D. thesis, Pennsylvania State University, 1988.

[29] P.-E. Janolin, J. Mater. Sci. **44**, 5025 (2009).

[30] A. K. Tagantsev, L. E. Cross, and J. Fousek, *Domains in Ferroic Crystals and Thin Films* (Springer, New York, 2010).

[31] A. Tagantsev, P. Muralt, and J. Fousek, Mater. Res. Soc. Symp. Proc. **784**, 517 (2004).